Article

Microfluidic Study of Enhanced Deposition of Sickle Cells at Acute Corners

Etienne Loiseau,[1] Gladys Massiera,[1] Simon Mendez,[2] Patricia Aguilar Martinez,[3] and Manouk Abkarian[1,4,*]
[1]Centre National de la Recherche Scientifique UMR 5221, Laboratoire Charles Coulomb and [2]Centre National de la Recherche Scientifique UMR 5149, Institut de Mathématiques et de Modélisation de Montpellier, Université de Montpellier, Montpellier, France; [3]Faculté de Médecine, Laboratoire d'Hématologie, Hôpital Saint Eloi, The Cardiovascular Health Research Unit de Montpellier, Montpellier, France; and [4]Centre National de la Recherche Scientifique UMR 5048-UM–Institut National de la Santé et de la Recherche Médicale UMR 1054, Centre de Biochimie Structurale, Montpellier, France

ABSTRACT Sickle cell anemia is a blood disorder, known to affect the microcirculation and is characterized by painful vaso-occlusive crises in deep tissues. During the last three decades, many scenarios based on the enhanced adhesive properties of the membrane of sickle red blood cells have been proposed, all related to a final decrease in vessels lumen by cells accumulation on the vascular walls. Up to now, none of these scenarios considered the possible role played by the geometry of the flow on deposition. The question of the exact locations of occlusive events at the microcirculatory scale remains open. Here, using microfluidic devices where both geometry and oxygen levels can be controlled, we show that the flow of a suspension of sickle red blood cells around an acute corner of a triangular pillar or of a bifurcation, leads to the enhanced deposition and aggregation of cells. Thanks to our devices, we follow the growth of these aggregates in time and show that their length does not depend on oxygenation levels; instead, we find that their morphology changes dramatically to filamentous structures when using autologous plasma as a suspending fluid. We finally discuss the possible role played by such aggregates in vaso-occlusive events.

INTRODUCTION

Sickle cell anemia (SCA) is an inherited hemoglobinopathy (1) affecting millions of people worldwide (2). It is caused by a point mutation resulting in the production of abnormal hemoglobin called hemoglobin S (HbS) (3). When deoxygenated, HbS molecules polymerize into long fibers (4), which can span the size of the red blood cell (RBC), distorting it into the classical crescent shape at rest (5,6). Such polymerization reduces the deformability of RBCs and reduces their lifespan (7–9), leading to anemia.

Originally, the stiffening of RBCs has been blamed for possibly causing vaso-occlusive events, qualifying SCA as a hemorheological disease (10,11). In this scenario, the obstruction process would be a competition between hydrodynamic forces that push the cells through the smallest capillaries to provide oxygen to the tissues and the polymerization of the fibers that occlude further transport of blood cells either by steric confinement in smaller capillaries (12), or by collective jamming of larger postcapillary venules (10,11), due to the loss of RBCs deformability and blood rheo-thickening.

However, during the last three decades, the pathophysiology of vaso-occlusion has proven to be more complex (13,14). While nearly all patients with SCA demonstrate chronic anemia, the clinical expression of the disease differs from one patient to another. It is now well admitted that vaso-occlusive events depend not only on the mechanical properties of circulating sickle red blood cells (SRBCs) but also on their ability to adhere to each other and to the vascular walls, an ability that is dependent upon inflammatory and oxidative stresses (15–17)).

Surprisingly, the role of the geometry where the vaso-occlusive events takes place has not been explored up to now. The microcirculatory network is highly branched and has a reticulated nature, because it is designed to perfuse efficiently and deeply into tissues. In these microcapillaries, 80% of the total pressure-drop between the aorta and the vena cava occurs (18), making it a critical place for disturbances. In addition, such microvessels generally present strong bends and wavy shapes, with short segment lengths between bifurcations, which tends to attenuate the formation of a cell-depleted layer adjacent to the vessels wall (19). These features could play a major role in vaso-occlusion when coupled to the adhesive properties of SRBCs. Even though the structure and geometry of the microcirculatory network has been poorly documented in SCA patients, preliminary results in the skeletal muscle of patients with sickle cell trait (20), in the liver (21), or in the conjunctival microcirculation (22) of patients with Sickle Cell Disease indicate important changes: a rarefaction of microvessels in the network, a decrease of their tortuosity, and an enlargement of their diameter. These characteristics all point to a physiological relevance that remains to be understood in the context of RBC adhesion, stiffening, and flow. There is a clear need to integrate both the rheological and the adhesive points of view in a more unified vision and to study the vaso-occlusion dynamics both at the cellular scale and in flow,

Submitted October 10, 2014, and accepted for publication April 14, 2015.
*Correspondence: manouk.abkarian@univ-montp2.fr
Editor: Cecile Sykes.

0006-3495/15/06/2623/10 $2.00
http://dx.doi.org/10.1016/j.bpj.2015.04.018

because the problem of obstruction is in essence a circulatory one.

We used microfluidic channels as a first step to explore the potential effects of flow geometry coupled to adhesion and polymerization on vaso-occlusion. We focused our attention to test the jamming scenario of vaso-occlusion in straight channels by designing microchannels with gas exchange that mimic physiological conditions of the microcirculation in terms of flow velocity, oxygen concentration, and hematocrit. While none of our experiments in straight channels showed clogging at physiologically relevant velocities, we observed intense deposition of SRBCs and the formation of SRBCs aggregates around acute corners where the flow changes rapidly, in a direction typical of bifurcations in vivo. Such aggregates might play a major role in vaso-occlusive events, linking adhesive properties of the membrane of the cells with flow characteristics.

MATERIALS AND METHODS

Blood samples

Blood samples were collected during the normal course of patient care at the Montpellier University Hospitals Hematology Laboratory (Montpellier, France), according to a research protocol (IRB 12/12-04) approved by the Partners Healthcare Institutional Review Board. Blood is collected in EDTA tubes, and the Mean Corpuscular Hemoglobin Concentration (MCHC) as well as the HbS percentage were determined by the hematology laboratory. All the samples containing HbS came from seven different patients with a homozygous genotype (HbSS) just before their exchange transfusion. The samples used in this study and their properties are listed in Table 1. RBCs are washed by successive centrifugation in a PBS (phosphate-buffered saline) solution containing 5 mM glucose, the final osmotic pressure being adjusted to 300 mOsm. RBCs are then resuspended at 50% hematocrit. In order to get samples with a narrow MCHC, RBCs are separated according to their density (and therefore according to the hemoglobin concentration) on a discontinuous Percoll (Cat. No. 77237; Sigma-Aldrich, St. Louis, MO) density gradient, following a protocol adapted from Corbett et al. (6). The gradient is centrifuged at 4000 g for 1 h at 4°C and then, SRBCs settling between the Percoll layers of density 1.092 and 1.101 (corresponding to a MCHC of 0.34 g/cm^3) were harvested with a micropipette. To get rid of the Percoll, the SRBCs are washed five times in a PBS + 5 mM glucose solution adjusted to 300 mOsm and finally resuspended at 50% hematocrit for storage at 4°C. Blood samples were used within a maximum of five days after venipuncture. Before any experiment, the SRBCs were diluted to a hematocrit value of 25% typical of the physiological microcirculation.

TABLE 1 List of blood samples used during the experiments

Sample	% HbS	Extra Free HbS	Autologous Plasma	Patient	Test
1	79.7	no	no	patient 1	clogging
2	59.2	no	no	patient 2	clogging
3	58.6	no	no	patient 3	clogging
4	57.9	no	no	patient 4	aggregate formation
5	69.0	no	no	patient 5	aggregate formation
6	0	yes	no	healthy 1	aggregate formation
7	58.2	no	yes	patient 4	aggregate formation
8	62.8	no	no	patient 6	aggregate formation
9	90.0	no	no	patient 7	aggregate formation
10	0	no	no	healthy 1	control (no HbS)
11	0	no	no	healthy 2	control (no HbS)
12	0	no	no	healthy 3	control (no HbS)

Samples for experiments that address the question of the presence of free HbS in solution were prepared using healthy RBCs washed as previously described. Before the experiment, RBCs were suspended in a buffer that consisted of a 3-day-old supernatant of washed SRBC sample (PBS + 5 mM glucose at 300 mOsm), containing a small amount of free HbS in solution, due to hemolysis (sample 6).

Samples used to investigate the effects of plasma proteins, platelets, and white blood cells were prepared from washed SRBCs that are suspended in autologous plasma containing platelets and white blood cells. The resulting white blood cell count was estimated by visual counting under a microscope and was ~0.1%.

Microfluidic channels

Devices are fabricated using the classical soft-lithography with replica molding method (23) (the detailed procedure is described in the Supporting Material). We mold the devices using a silicone elastomer, PDMS (polydimethylsiloxane), which is porous to gases (24). We use this feature to control the oxygen concentration in the channels via a two-layer PDMS structure. The first layer of 60 μm in thickness is engraved with channels of 30 μm in height where RBCs should flow. This layer is bonded to a glass microslide by plasma bonding. The plasma treatment has to be fast (few seconds) because of the fast decrease of permeability of PDMS with exposure time to the corona discharge (25). The second layer, dedicated to the gas flow, is plasma-bonded on the top of the first one and engraved with a long serpentine channel of 500 μm in width and 80 μm in height. It covers the entire surface of the chip (see Fig. 1) to maximize gas exchange. RBC channels and gas channels are thus separated by a 30-μm-thick PDMS membrane through which oxygen diffuses. The geometries of the microfluidic chips are shown in the Fig. 1. They all contain a deoxygenation chamber that consists of a large, rectangular, 2-cm-long and 4-mm-wide section, supported by pillars to prevent the top surface from collapsing onto the glass slide. Downstream from the deoxygenation chamber, we have the microcirculation section. On the first chip (chip 1), the microcirculation section consists of a region containing triangular pillars to mimic corner flows, followed by a section of sixteen 1-cm-long and 30-μm-wide parallel channels (see Fig. 1 *b*) to test the clogging hypothesis. On the second chip (chip 2), the microcirculatory section consists of successive branchings of 20-μm-wide channels (Fig. 1 *c*).

RBCs deoxygenation protocols

To optimize the deoxygenation rate, the gas exchange surface is large, with a 30-μm-thick membrane separating the gas channels from the flow of RBCs. In such a device, gas exchange is known to occur over tens of seconds (24,26,27). This timescale has to be compared with the time for a RBC to flow along the deoxygenation chamber, which is of the order of minutes. When the RBCs reach the microcirculatory part, they are already deoxygenated if pure nitrogen is injected in the serpentine channel. To saturate the PDMS chip, we initiated the gas flow 30 min before the injection of RBCs. The gas flow is maintained throughout the experiment. RBCs are therefore deoxygenated while flowing.

Experimental setup

Observations are performed on an inverted microscope and the temperature surrounding the microfluidic chips is maintained at 37°C by an air flow in all experimental conditions. The gas channel is directly linked to a pressure controller (Fluigent-4C, four independent channels; Fluigent, Lowell, MA) and RBCs are injected from a pressurized tube that is linked to the pressure

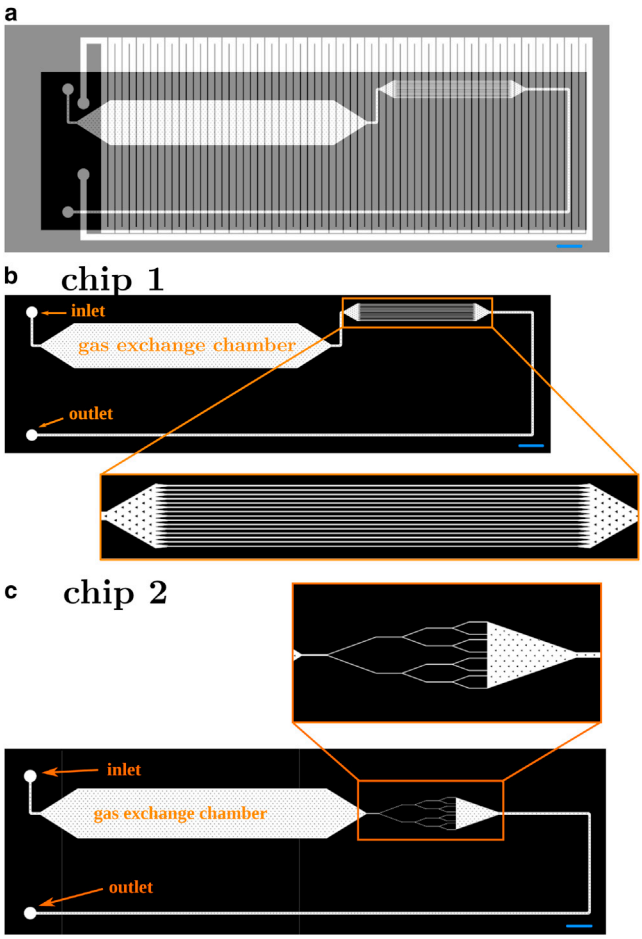

FIGURE 1 Microfluidic channel geometry. (*a*) Overlay of the geometry of the gas channel (*light gray*) and the channel network for the RBC suspension (*black*). The gas channel, a 500-μm-wide and 100-μm-high coil, covers the entire surface of the chip to promote and control gas exchange within the RBC channels. (*b*) Geometry of RBC channels of chip 1. RBCs are deoxygenated during their flow through the gas exchange chamber. In the zoom-in window, microcirculation section consisting of a region of triangular pillars followed by sixteen 1-cm-long and 30-μm-wide parallel channels. (*c*) The microcirculation section consists of 20-μm-wide channels that successively branch, for chip 2. Scale bars, 2 mm. To see this figure in color, go online.

controller. Microfluidic channels have been designed to obtain a configuration with characteristic length, velocity, and hematocrit conditions similar to that encountered in the microcirculation (18). The total pressure difference used to induce the flow is 130 mbar. Given the typical length of the devices we use, this value yields a pressure drop per unit length of ~0.1 Pa/μm, typical of the microcirculation (28). Characteristic velocities of RBCs measured in the middle plane of the 30-μm channels are, depending on this input pressure, of ~7 mm/s to mimic the postcapillary venules blood circulation (28). Around the triangular pillars studied here, the velocity ranges from 100 to 400 μm/s, closer to capillary flow velocities (29).

RESULTS AND DISCUSSION

We first test the clogging hypothesis at the microcirculation scale using chip 1. While no occlusion has been observed in the 30-μm-wide microchannels, even after 2 h of flow, we observe the deposition of SRBCs into large aggregates at acute corners in the microfluidic device. These aggregates contain both SRBCs and healthy RBCs, because our samples are all from exchange transfusion patients. Nevertheless, we verified that neither healthy nor sickled RBCs enter the microchannels as clusters; and as we will show later, neither deposition nor aggregation in flow occurs only with healthy RBCs.

Role of the flow geometry

We focus our attention on the triangular pillars whose acute corners both upstream and downstream mimic locally the fast variation of direction of the streamlines observed at bifurcations in the microcirculation. We observe the formation of SRBCs aggregates on one pillar first at the two corners situated downstream (chip 1) and later at the opposite corner upstream (chips 1 and 2) as shown in Figs. 2, *a–c*, and 3. The deposition is slow and a delay time of 20 min is observed before the onset of growth, which results from successive and accumulative adhesion of SRBCs. The cells form layers and the flow pushes slowly the whole aggregate on each side toward the center of the triangular pillar base. This leads to the formation of a single large aggregate after ~1 h of flow (Fig. 2 *c*; Movie S1 in the Supporting Material). Deposition at the upstream front of the pillar results in the formation of an aggregate on each side (Fig. 3, *a–c*). This deposition is observed to be slower than the one downstream. When observed in branching channels (chip 2), these aggregates reach a critical transverse size up to one-half of the total channel width (Fig. 3 *d*). This is due to a continuous increase of the shearing force during deposition due to channel lumen reduction. Above this critical size, we observe some additional SRBCs that transiently bind to the aggregate with a residence time ranging between 2 and 13 s. The intricate interaction between the flow and the aggregate development at branches leads us to focus this study of deposition around the pillars walls where the flow is not confined.

Interestingly, no deposition is initiated on the substrate or the ceiling of the chips on the timescale of the experiments. Deposited aggregates are observed waving in the flow and are found to be best focused around the half-height of the channel. They can break or detach from the pillars, but this remains a rare event.

We characterize the temporal evolution of the size of different SRBCs aggregates at the rear of the pillars using samples 4, 8, and 9 at 25% hematocrit (similar to venules hematocrit), as shown in Fig. 2 *g*. SRBCs are deoxygenated while flowing. Initially, only a few RBCs adhere behind the pillar, and during 15–20 min there is no major evolution. Then, an aggregate develops from each corner of the triangular pillar and finally merge after 1 h. This sequence is shown for sample 4 in Fig. 2, *a–c*. The resulting aggregate still grows to reach a steady length of several tens of microns. The aggregate redefines the boundary of the

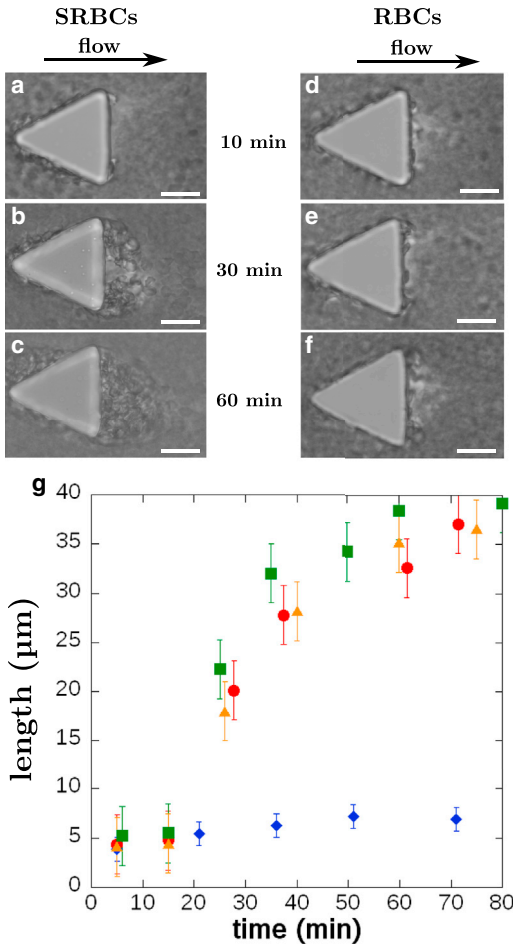

FIGURE 2 Morphology and time evolution of aggregates at the rear of pillars. (*a–c*) SRBCs from sample 4: pictures of aggregate formation at the rear of a pillar. For $t = 10$ min, only a few cells are in adhesion on the PDMS pillar. After 30 min, an aggregate has grown on both corners at the rear of the pillar. After 60 min, the two aggregates merge and the length remains stable. Scale bars, 20 μm. (*d–f*) Healthy RBCs deposition on pillars (sample 10). Only a few cells stick to the pillar. Scale bars, 20 μm. (*g*) Temporal evolution of the length of SRBCs aggregate at the rear of pillars (sample 4, *red circle*; sample 8, *orange triangle*; sample 9, *green square*; 25% hematocrit). The aggregate length is defined as the maximum extent from the base of the pillar and the fluctuating end. For $t < 15$ min, only a few cells are in adhesion on the PDMS pillar. Then the growth initiates and aggregates can reach a size of ~40 μm. For each curve, the length is averaged over seven different aggregates. Control experiment, with healthy RBCs: only few of them stick to the PDMS pillar (*blue diamonds*, sample 10, 25% hematocrit). To see this figure in color, go online.

triangular pillar, reducing the local curvature of the streamlines and hindering further deposition. The aggregate length saturates when the angle of the corner that is initially close to 60° reaches ~120°. Control experiments were performed on the same timescales with healthy RBCs (same MCHC). They show that only a few RBCs stick at the corners of the pillars (*blue curve* in Fig. 2 *g*; pictures in Fig. 2, *d–f*, and Fig. S2 in the Supporting Material).

Our microfluidic assay points out that acute corners are a location of much higher capture frequency and a place for aggregates to grow, as also observed for biofilm growth of dilute solutions of bacteria (30). The formation of SRBCs aggregates on the vertical walls of the pillars, where the flow changes direction, is to be correlated with the few in vivo images of the onset of deposition available in the literature (31–33). In these studies, aggregates are present at blood vessel bifurcations where strong bends are present, similar to the flow geometry around the triangular pillars in our microfluidic chips.

The hydrodynamics of concentrated suspensions around corners at low Reynolds number seems to play a fundamental role in the cellular deposition. To describe the flow in this region, we use cross-correlation image velocimetry (using the software IMAGEJ, National Institutes of Health, Bethesda, MD, and its particle image velocimetry plugin) around one pillar to obtain the local average velocity field and the associated streamlines for SRBCs flowing in the middle plane of the channel. The streamlines are reported in Fig. 4 *a*, together with the trajectories for seven SRBCs followed by hand at different initial distances from one of the pillar edge. We compare these lines with those of the suspending fluid flow only (without cells, *white streamlines* in Fig. 4 *a*), computed using an in-house three-dimensional flow solver (34) (YALES2BIO, details in the Supporting Material) around a pillar of the same geometry. The creeping flow (the Reynolds number is ~0.0028) is computed around an infinite array of pillars, using periodic conditions in the directions tangential to the wall. The comparison reveals that downstream of the pillar, the SRBCs streamlines are contracted toward the pillar basis compared to the three-dimensional computed flow of a simple Newtonian fluid in the same geometry. On average, there is a net transverse drift of the cells toward the base (on each side of the pillar) in the region of maximum rotation of the streamlines. This observation could explain the higher collision rate of the SRBCs in this region leading to a higher deposition rate. Furthermore, the cells can explore the otherwise excluded region behind the pillar around the corner. Deformable objects such as RBCs circulating near a flat wall are known to be driven away from the wall by a lift force (35,36) at the origin of the cell-free layer in the microcirculation. This force prevents RBCs from adhering to vessels wall. This is not the case here, notably due to the presence of corners and multibody interactions. The contraction of the streamlines we see, compared to the three-dimensional Newtonian case, seems to indicate the non-Newtonian nature of this effect.

To illustrate the link among flow geometry, inverse-lift, and multibody interactions, we perform complementary simulations of one and two deformable two-dimensional capsules flowing around a pillar using our in-house flow solver. The capsules are supposed to be inextensible and resist bending. Their dynamics and deformation is computed using a full fluid-structure interaction approach and results are displayed in Fig. 4, *b* and *c*. All the technical

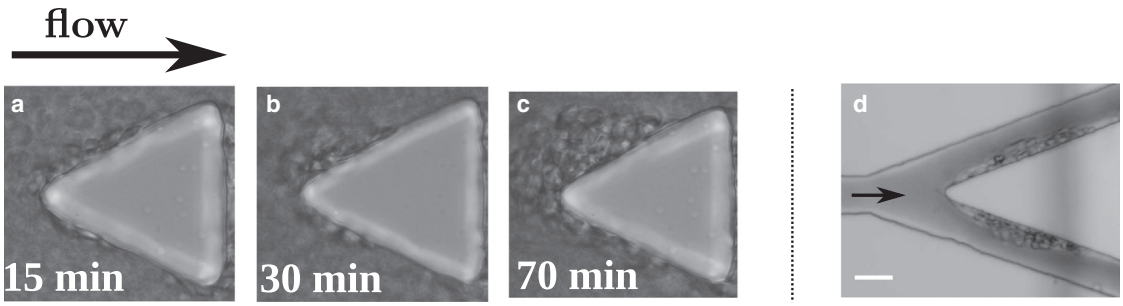

FIGURE 3 Morphology of SRBC aggregates at the front of pillars. (*a–c*) Aggregation over time at the front of a pillar (sample 4). (*d*) Aggregate at a branching point in 20-μm-wide channels (geometry Fig. 1 *c*), observed after 2 h of flow. In this geometry, the aggregate can grow up to half of the channel width (sample 5). Scale bars, 20 μm.

details and assumptions are provided in the Supporting Material. In the case of a single capsule, the shortest distance between the capsule membrane and the wall always increases, except at the corner, where the flow slightly accelerates. On the other hand, a capsule may follow a different trajectory if a second capsule follows it. In the corner case displayed in Fig. 4 *b*, the front capsule stays closer to the corner and remains close to the pillar wall beyond the corner in a zone of lower speed. If the cells are close to each other at the right moment when passing the corner, their hydrodynamic collision produces a transitory pairing (due to lubrication forces) that drives the cluster in an otherwise forbidden region during rotation. We then compared this situation with a second test case shown in Fig. 4 *c* with the same capsules in a simple two-dimensional Couette flow between two flat walls (configuration shown in Fig. S5 *b*). The model, grid resolution, and the characteristic parameters (shear rate, capillary number, Reynolds number, bending coefficient) are strictly identical to the case of flowing capsules around a pillar. In this Couette flow, the shear rate is constant and identical to the one seen by the capsules when they flow along the lateral wall of the pillar. Couette flow simulations were used as control cases, to confirm that the specific results obtained around the pillar are related only to the flow geometry. In the Couette flow, capsules simply interact by switching positions, as observed in computations of two interacting vesicles or capsules (37) in the presence of a wall. The specific phenomenon shown in the article of capsules exploring regions very close to the pillar wall is thus the result of a combination between geometrical characteristics of the corner and multibody effects. This behavior increases the probability for the cells to stick to each other and to adhere at this specific location, and may participate in the formation of an aggregate at the corner.

In general, it has been demonstrated that the highly bifurcating topology of the microcirculatory network causes RBCs from side branches to be frequently introduced into the region closest to the wall at each branch, as shown for instance in the vascular bed of the rat spinotrapezius muscle (19), preventing the development of a significant cell free layer in networks. This phenomenon is also observed in vitro around our pillars or at our microfluidic bifurcations. Such modifications would also promote adhesion, but further studies both in vitro and in vivo are necessary to understand how flow patterns such as the bifurcation angle and flow direction could promote deposition and lead to occlusion.

Role of oxygen

We test the role of oxygen on the formation of aggregates using chip 1 (Fig. 5). Starting from a long aggregate formed under deoxygenated conditions, we replace the nitrogen in the gas channel with air. First, the aggregate becomes more floppy due to the depolymerization of HbS within the SRBCs. Second, the cells detach and the aggregate shortens during 10 min. Then, third and finally, the aggregation process restarts in oxygenated conditions and the aggregate recovers the same size reached under nitrogen conditions. More generally, oxygen does not prevent aggregate formation at the pillar corners. Indeed, when we initiate the flow under oxygenated conditions, we observe the growth of RBC aggregates of the same size, in contrast to those found in the absence of oxygen (see Fig. S3). It is interesting to notice that aggregates made of oxygenated SRBCs exhibit a different appearance as well. Oxygenated SRBCs are more deformable due to the absence of HbS polymer and thus, they better align, according to the streamlines, into layered stacks of cells (Fig. 5 *d* and Movie S2). Notable, as in the deoxygenated case, the aggregate surrounds the pillar, reducing locally the curvature and hindering further growth.

Role of the presence of free hemoglobin and the products of hemolysis

People suffering from sickle cell anemia have a higher amount of free hemoglobin in their blood plasma due to a higher intravascular hemolytic rate (38). Furthermore, some studies report on the possibility for hemoglobin to bind to the RBC membrane (39,40). We investigate in this section whether the presence of products of hemolysis

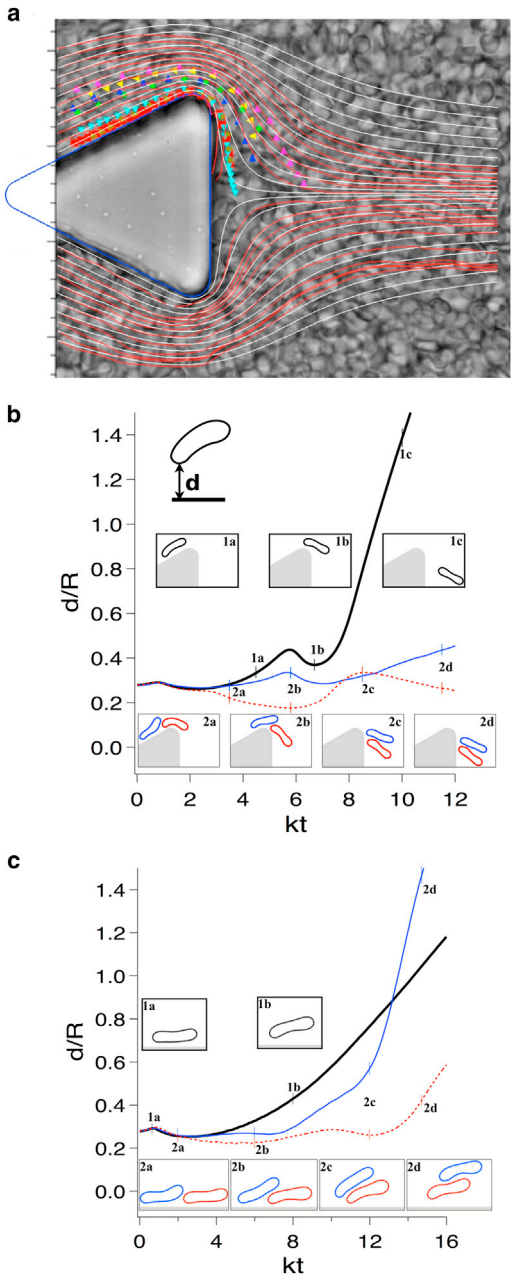

FIGURE 4 SRBCs flow around corners. (*a*) (*Triangle symbols*) Individual trajectories of SRBC. (*Red streamlines*) SRBC flow field computed by particle image velocimetry. The SRBC flow field contracts at the rear of the pillar compared to the creeping flow of a Newtonian fluid (*white streamlines*). (*b*) Simulation of deformable two-dimensional capsules flowing around a corner: the distance d of a capsule to the pillar wall, normalized by the capsule characteristic size R, is represented over time. The comparison between the trajectory of a single capsule (*black curve*) and trajectories of two consecutive capsules (*red* and *blue curves*), points out multibody effects: in the displayed case, consecutive capsules flow closer to the corner wall than a single capsule. Moreover, when two consecutive capsules flow around the corner, the second capsule may push the first one closer to the wall at the corner (*inset 2 b*) and at the rear (*inset* 2 *d*), as in the simulation shown here. (*c*) Simulation of deformable two-dimensional capsules flowing along a flat wall in a Couette flow: same legend as (*b*). To see this figure in color, go online.

(PHemo), which contain free HbS, could be an enhancing factor for the formation of cellular aggregates. In the channels, we inject healthy RBCs suspended at 25% hematocrit in the supernatant of initially washed SRBCs samples kept in the fridge (PBS + 5 mM glucose + PHemo; see Materials and Methods), which contains free HbS due to hemolysis (sample 6). The evolution of the average aggregate length over time is then reported in Fig. 6. Aggregates grow after ~20 min, as previously observed in the case of SRBCs, but reach a constant length of 18 $\pm$ 1.5 μm after 80 min, three times shorter than for the SRBCs aggregates. When the same experiment is performed with RBCs suspended in a supernatant of healthy RBCs (see Materials and Methods) containing free HbA instead of free HbS and all the same products of hemolysis, we do not observe aggregate formation similar to the former case (*blue curve* in Fig. 6).

Free HbS and its derivative products seem to play a role in the adhesive nature of RBCs. However, this is not sufficient to obtain aggregates on the order of 50 μm. HbS is usually submitted to a high rate of autooxidation, particularly when it is not encapsulated in RBCs. The generation of oxygen free radicals may cause severe RBCs membrane damage, hence changing the rheological and adhesive properties of flowing RBCs. It was previously reported that oxidative stress is able to decrease RBCs deformability (41), increase RBCs aggregation strength, and promote the adhesion of RBCs to endothelial cells (42,43). Indeed, it may be speculated that increased adhesion and RBC aggregate formation at a corner in the presence of free HbS could be related to increased oxidative stress. These questions need further investigation in order to better understand the proadhesive properties of SRBCs.

Effect of autologous plasma in combination with platelets and white blood cells

Since the 1990s, numerous factors have been identified as potentially involved in vaso-occlusive mechanisms (14,17). These include the presence of proteins in the plasma, platelets, and WBCs. We explore the potential role of these elements on the aggregate formation in our microfluidic chips by adding autologous plasma containing platelets and WBCs to SRBCs (blood sample 7). The final WBCs count was ~0.1%. We observe the formation of cellular aggregates but the morphology is completely different. In this case, aggregates form long chains, waving in the flow, which can reach several hundreds of microns (Fig. 7 *b* and Movie S3). SRBCs in these aggregates are elongated and adopt a tear drop shape, forming tethers. On Fig. 7, we can distinguish the membrane tube linking the pillar to the first RBC as well as a WBC in the aggregate. Contrary to previous observations, the growth of these aggregates appears to be randomly distributed in time. They can form within the first minutes of flow and on a timescale of seconds. In the control experiment with healthy cells, we do not obtain such structures.

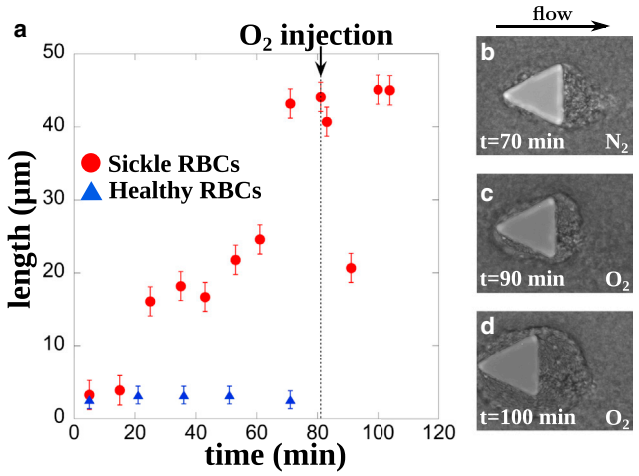

FIGURE 5 Oxygen does not prevent aggregate formation. (*a*) Time evolution of SRBCs aggregates at the rear of a pillar in the absence or presence of oxygen (sample 4). Under deoxygenated conditions, the aggregate grows as previously described, to reach a stable length of 45 μm. Then, nitrogen is turned off in the gas channel and replaced by oxygen at $t = 80$ min. HbS polymer in SRBCs depolymerizes, which results in more deformable SRBC and a rearrangement of the aggregate. The length of the aggregate decreases to 20 μm before recovering its initial length 20 min after oxygen injection. (*b–d*) Snapshots of the aggregate morphology in presence or absence of oxygen; the time refers to the evolution in (*a*). Blood sample number 4 at 25% hematocrit is used. Results of a control experiment with healthy RBCs are also shown (*blue triangles*, sample 10). To see this figure in color, go online.

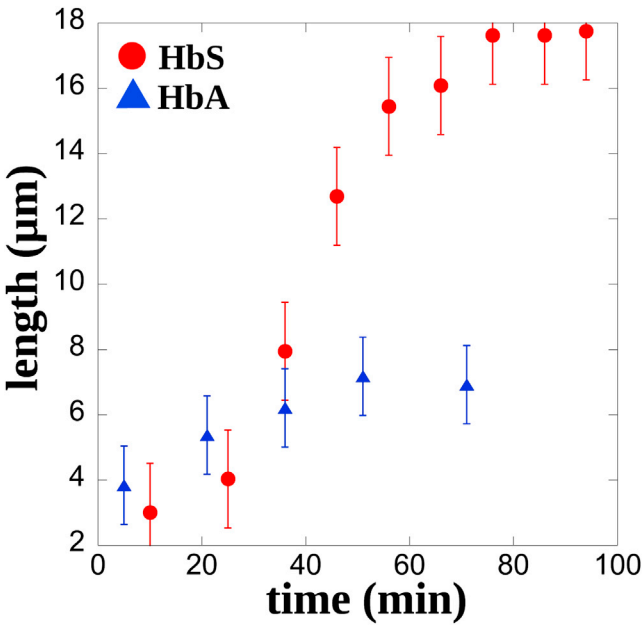

FIGURE 6 Free HbS promotes aggregation. Evolution of aggregates for healthy RBCs flowing in a medium that contains free HbS (blood sample 6, *red circles*) and for healthy RBCs with free HbA in solution (*blue triangles*). The length is an average over 10 aggregates. To see this figure in color, go online.

We still do not know the respective role of platelets or WBCs in the formation of these structures and the origin of the membrane forming the filaments. However, recent observations show a preferential adhesion of WBCs at bifurcations (44), independent of the endothelium state, which could result from local hydrodynamical conditions. In addition, RBCs-WBCs interactions are known to be important in postcapillary venules (32) and WBCs from SCA patients seem to be more adhesive to SRBCs (45) and are capable of forming aggregates of few cells in whole blood (46). Moreover, the drastic morphology change we observe for the aggregate could be correlated to the known activation of platelets observed during blood storage at 4°C (47,48). It has been reported in particular that activated platelets are able to form aggregates in a shear microgradient (49), in locations analogous to the corner of the pillars of this device, but for much higher Reynolds number flow conditions, not relevant for the microcirculation. Further experiments are required to determine the specific role of the platelets or WBCs during aggregate formation. A first step would be to label their membrane with different dyes to track their positions within an aggregate.

Vaso-occlusion: two hypothetical scenarios

All the observations reported above provide information to propose two hypothetical scenarios for vaso-occlusion to occur at bifurcations in vivo, as illustrated in Fig. 8 *a*. Aggregation present at corners could either reduce vessels' diameter (as seen at bifurcations in Fig. 3 *d*) until occlusion, and/or large aggregates could be shed randomly in time disturbing the flow downstream. We observed in rare occasions the breaking of the aggregate (Fig. 8 *b* and Movie S4) and its passage through a 30-μm channel. We succeeded in recording one passage event in a slightly different chip where the region of 30-μm channels was replaced by an array of 20-μm channels flowing at different intersection angles into a main output channel (see geometry in the Supporting Material). This passage is shown in Fig. 8 *c*. When the aggregate enters upstream of the field of view, the entire flow in the channel decreases. When the aggregate reaches the field of view, we observe downstream of it a depletion in SRBCs, while upstream the SRBCs density is higher. This critical situation leads to a dramatic drop of the average flow velocity (down to 15% of its initial value as shown in Fig. 8 *c*), and could promote further HbS polymerization and aggregation of the SRBCs behind the aggregate. This would lead to flow regimes close to the ones where jamming was observed in microfluidic devices (26). However, we were never able to observe total occlusion in our devices, but this is consistent with the fact that blood samples came from patients that are regularly transfused to prevent frequent vaso-occlusive crises. In addition, other factors listed by Switzer et al. (38) such as platelets aggregation, vasoconstrictive molecules (endothelin family proteins), and decreased nitric oxide bioavailability, will certainly

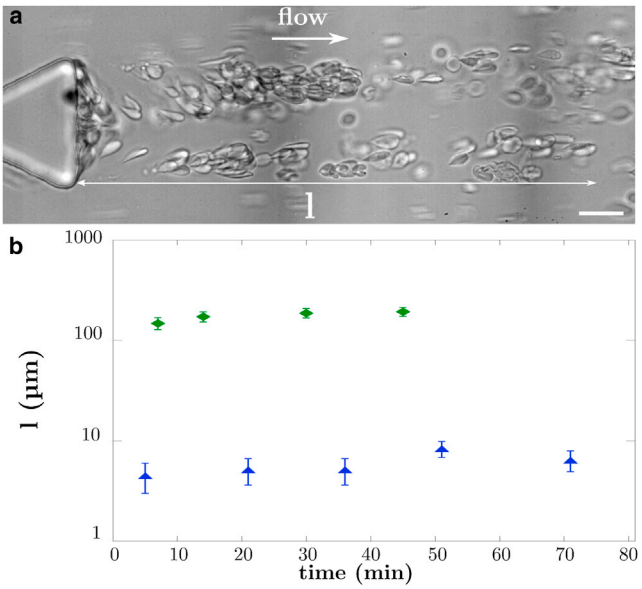

FIGURE 7 Morphology of SRBCs aggregate in the presence of autologous plasma, platelets, and WBCs. (*a*) SRBCs from sample 7. The aggregates are long chains fluctuating in the flow. They can reach several hundreds of microns long. We can distinguish the membrane tube linking the pillar and the first RBC. The picture has been taken after the RBCs had cleared the channel but there is still some media flowing in the channel. This allows a better observation of the aggregate structure. The term *l* defines the length of the aggregate. Scale bar, 20 μm. (*b*) Aggregates' length in presence of autologous plasma, platelets, and $\simeq$0.1% WBCs, sample 7 (*green diamonds*). The control corresponds to healthy RBCs (*blue triangles*, sample 10). To see this figure in color, go online.

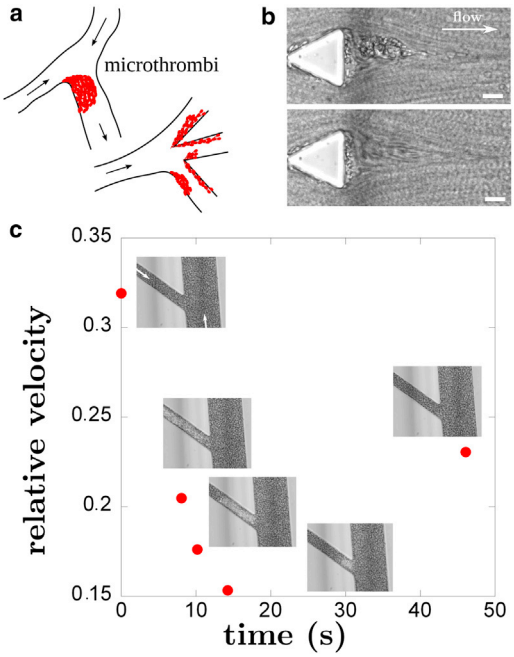

FIGURE 8 Suggested scenario. (*a*) The formation of microthrombi at a corner or at branching points can drastically impair the hemodynamics, due to a possible severe restriction of the lumen area. (*b*) Example of aggregate detachment (blood sample 8 at 25% hematocrit): when reaching a critical size, cellular aggregates can break. Scale bar, 20 μm. (*c*) Free flowing aggregate in microcirculation. Relative velocity of an aggregate flowing along a 20-μm-wide channel. Initial velocity is 200 μm/s and SRBCs were from blood sample 8 at 25% hematocrit. (*Open arrows*) Direction of the flow. To see this figure in color, go online.

act together with the hydrodynamic conditions at corners to promote deposition and aggregation of SRBCs and to participate in a vaso-occlusive crisis.

CONCLUSIONS

Microfluidics is a suitable tool to study blood circulation at the microcirculatory level. In this study, we reported on SRBCs' aggregation at bifurcations and around acute corners. We have shown that the geometry of the flow is a key factor for the formation of SRBCs aggregates. The onset of aggregation results from an intricate interplay among geometry, collective motions, and proadhesive properties of SRBCs, and remains to be fully explored and understood.

Moreover, the origin of SRBCs' adhesiveness at the heart of our observations is still an open question, and measuring the strength of adhesion would give some better insights on its importance in the context of cellular deposition in flow. In addition, it would be interesting to extend this microfluidic study to different hematocrit and healthy/sickled RBCs proportions, as well as to research actively the signs of such corner-flow-enhanced deposition and aggregation in vivo and its consequences on vaso-occlusion.

Finally, we hope that our preliminary results will motivate future studies on the role of flow geometry in cell capture not only during vaso-occlusion but also in other physiologically relevant situations like the inflammatory response.

SUPPORTING MATERIAL

Supporting Materials and Methods, six figures, and four movies are available at http://www.biophysj.org/biophysj/supplemental/S0006-3495(15)00397-5.

AUTHOR CONTRIBUTIONS

E.L., G.M., and M.A. designed the study; E.L. realized the experiments; and S.M. performed the numerical simulations. All the authors discussed the results and wrote the article. The authors declare no competing financial interests.

ACKNOWLEDGMENTS

Vincent Moureau and Ghislain Lartigue from the CORIA lab, and the personnel from the SUCCESS scientific group, are acknowledged for providing the YALES2 code, on which YALES2BIO is based. UMR 5221 belongs to the Centre National de la Recherche Scientifique French Consortium CellTiss. We would like to thank both A. Bala Subramaniam and P. Connes for reading and correcting the manuscript. P. Connes is also acknowledged for our fruitful discussions on SCA.

This work was supported by the French Ministry of Research, the Centre National de la Recherche Scientifique Physics-Chemistry-Biology Interdisciplinary Program, the Region Languedoc-Roussillon, the Agence Nationale de la Recherche (grant No. ANR-11-JS09-0011), the Labex Solutions Numériques, Matérielles et Modélisation pour l'Environnement et le Vivant (convention No. ANR-10-LABX-20), and the BPI France project DataDiag.

REFERENCES

1. Neel, J. V. 1949. The inheritance of sickle cell anemia. *Science.* 110:64–66.
2. Modell, B., and M. Darlison. 2008. Global epidemiology of hemoglobin disorders and derived service indicators. *Bull. World Health Organ.* 86:480–487.
3. Pauling, L., H. A. Itano, …, I. Wells. 1949. Sickle cell anemia a molecular disease. *Science.* 110:543–548.
4. Eaton, W. A., and J. Hofrichter. 1990. Sickle cell hemoglobin polymerization. *Adv. Protein Chem.* 40:63–279.
5. Christoph, G. W., J. Hofrichter, and W. A. Eaton. 2005. Understanding the shape of sickled red cells. *Biophys. J.* 88:1371–1376.
6. Corbett, J. D., W. E. Mickols, and M. F. Maestre. 1995. Effect of hemoglobin concentration on nucleation and polymer formation in sickle red blood cells. *J. Biol. Chem.* 270:2708–2715.
7. Evans, E. A., and N. Mohandas. 1987. Membrane-associated sickle hemoglobin: a major determinant of sickle erythrocyte rigidity. *Blood.* 70:1443–1449.
8. Du, E., M. Diez-Silva, …, S. Suresh. 2015. Kinetics of sickle cell biorheology and implications for painful vasoocclusive crisis. *Proc. Natl. Acad. Sci. USA.* 112:1422–1427.
9. Nash, G. B., C. S. Johnson, and H. J. Meiselman. 1984. Mechanical properties of oxygenated red blood cells in sickle cell (HbSS) disease. *Blood.* 63:73–82.
10. Ballas, S. K., and N. Mohandas. 2004. Sickle red cell microrheology and sickle blood rheology. *Microcirculation.* 11:209–225.
11. Lamarre, Y., M. Romana, …, P. Connes. 2012. Hemorheological risk factors of acute chest syndrome and painful vaso-occlusive crisis in children with sickle cell disease. *Haematologica.* 97:1641–1647.
12. Mozzarelli, A., J. Hofrichter, and W. A. Eaton. 1987. Delay time of hemoglobin S polymerization prevents most cells from sickling in vivo. *Science.* 237:500–506.
13. Hebbel, R. P. 1991. Beyond hemoglobin polymerization: the red blood cell membrane and sickle disease pathophysiology. *Blood.* 77:214–237.
14. Embury, S. H. 2004. The not-so-simple process of sickle cell vasoocclusion. *Microcirculation.* 11:101–113.
15. Hebbel, R. P., O. Yamada, …, J. W. Eaton. 1980. Abnormal adherence of sickle erythrocytes to cultured vascular endothelium: possible mechanism for microvascular occlusion in sickle cell disease. *J. Clin. Invest.* 65:154–160.
16. Hebbel, R. P., R. Osarogiagbon, and D. Kaul. 2004. The endothelial biology of sickle cell disease: inflammation and a chronic vasculopathy. *Microcirculation.* 11:129–151.
17. Hebbel, R. P. 2008. Adhesion of sickle red cells to endothelium: myths and future directions. *Transfus. Clin. Biol.* 15:14–18.
18. Popel, A. S., and P. C. Johnson. 2005. Microcirculation and hemorheology. *Annu. Rev. Fluid Mech.* 37:43–69.
19. Bishop, J. J., A. S. Popel, …, P. C. Johnson. 2001. Effects of erythrocyte aggregation and venous network geometry on red blood cell axial migration. *Am. J. Physiol. Heart Circ. Physiol.* 281:H939–H950.
20. Vincent, L., L. Féasson, …, L. Messonnier. 2010. Remodeling of skeletal muscle microvasculature in sickle cell trait and α-thalassemia. *Am. J. Physiol. Heart Circ. Physiol.* 298:H375–H384.
21. Bauer, T. W., G. W. Moore, and G. M. Hutchins. 1980. The liver in sickle cell disease. A clinicopathologic study of 70 patients. *Am. J. Med.* 69:833–837.
22. Cheung, A. T., P. C. Chen, …, T. Wun. 2002. Microvascular abnormalities in sickle cell disease: a computer-assisted intravital microscopy study. *Blood.* 99:3999–4005.
23. Duffy, D. C., J. C. McDonald, …, G. M. Whitesides. 1998. Rapid prototyping of microfluidic systems in poly(dimethylsiloxane). *Anal. Chem.* 70:4974–4984.
24. Vollmer, A. P., R. F. Probstein, …, T. Thorsen. 2005. Development of an integrated microfluidic platform for dynamic oxygen sensing and delivery in a flowing medium. *Lab Chip.* 5:1059–1066.
25. Shiku, H., T. Saito, …, H. Yamada. 2006. Oxygen permeability of surface-modified poly(dimethylsiloxane) characterized by scanning electrochemical microscopy. *Chem. Lett.* 35:234–235.
26. Higgins, J. M., D. T. Eddington, …, L. Mahadevan. 2007. Sickle cell vasoocclusion and rescue in a microfluidic device. *Proc. Natl. Acad. Sci. USA.* 104:20496–20500.
27. Polinkovsky, M., E. Gutierrez, …, A. Groisman. 2009. Fine temporal control of the medium gas content and acidity and on-chip generation of series of oxygen concentrations for cell cultures. *Lab Chip.* 9:1073–1084.
28. Lipowsky, H. H. 2005. Microvascular rheology and hemodynamics. *Microcirculation.* 12:5–15.
29. Pries, A. R., T. W. Secomb, and P. Gaehtgens. 1996. Biophysical aspects of blood flow in the microvasculature. *Cardiovasc. Res.* 32:654–667.
30. Rusconi, R., S. Lecuyer, …, H. A. Stone. 2011. Secondary flow as a mechanism for the formation of biofilm streamers. *Biophys. J.* 100:1392–1399.
31. Zennadi, R., B. J. Moeller, …, M. J. Telen. 2007. Epinephrine-induced activation of LW-mediated sickle cell adhesion and vaso-occlusion in vivo. *Blood.* 110:2708–2717.
32. Frenette, P. S. 2004. Sickle cell vasoocclusion: heterotypic, multicellular aggregations driven by leukocyte adhesion. *Microcirculation.* 11:167–177.
33. Kaul, D. K., M. E. Fabry, and R. L. Nagel. 1996. The pathophysiology of vascular obstruction in the sickle syndromes. *Blood Rev.* 10:29–44.
34. Mendez, S., E. Gibaud, and F. Nicoud. 2014. An unstructured solver for simulations of deformable particles in flows at arbitrary Reynolds numbers. *J. Comput. Phys.* 256:465–483.
35. Abkarian, M., and A. Viallat. 2008. Vesicles and red blood cells in shear flow. *Soft Matter.* 4:653–657.
36. Singh, R. K., X. Li, and K. Sarkar. 2014. Lateral migration of a capsule in plane shear near a wall. *J. Fluid Mech.* 739:421–443.
37. Narsimhan, V., H. Zhao, and E. S. G. Shaqfeh. 2014. Coarse-grained theory to predict the concentration distribution of red blood cells in wall-bounded Couette flow at zero Reynolds number. *Phys. Fluids.* 25:1–21.
38. Switzer, J. A., D. C. Hess, …, R. J. Adams. 2006. Pathophysiology and treatment of stroke in sickle-cell disease: present and future. *Lancet Neurol.* 5:501–512.
39. Aprelev, A., M. A. Rotter, …, F. A. Ferrone. 2005. The effects of erythrocyte membranes on the nucleation of sickle hemoglobin. *Biophys. J.* 88:2815–2822.
40. Shaklai, N., V. S. Sharma, and H. M. Ranney. 1981. Interaction of sickle cell hemoglobin with erythrocyte membranes. *Proc. Natl. Acad. Sci. USA.* 78:65–68.
41. Tomaiuolo, G. 2014. Biomechanical properties of red blood cells in health and disease towards microfluidics. *Biomicrofluidics.* 8:051501.
42. Hierso, R., X. Waltz, …, M.-D. Hardy-Dessources. 2014. Effects of oxidative stress on red blood cell rheology in sickle cell patients. *Br. J. Haematol.* 166:601–606.
43. Yedgar, S., D. K. Kaul, and G. Barshtein. 2008. RBC adhesion to vascular endothelial cells: more potent than RBC aggregation in inducing circulatory disorders. *Microcirculation.* 15:581–583.

44. Tousi, N., B. Wang, …, B. Prabhakarpandian. 2010. Preferential adhesion of leukocytes near bifurcations is endothelium independent. *Microvasc. Res.* 80:384–388.

45. Finnegan, E. M., A. Turhan, …, G. A. Barabino. 2007. Adherent leukocytes capture sickle erythrocytes in an in vitro flow model of vaso-occlusion. *Am. J. Hematol.* 82:266–275.

46. Chaar, V., J. Picot, …, W. El Nemer. 2010. Aggregation of mononuclear and red blood cells through an $\alpha_4\beta_2$-Lu/basal cell adhesion molecule interaction in sickle cell disease. *Haematologica.* 95:1841–1848.

47. Egidi, M. G., A. D'Alessandro, …, L. Zolla. 2010. Troubleshooting in platelet storage temperature and new perspectives through proteomics. *Blood Transfus.* 8 (*Suppl 3*):s73–s81.

48. Kaufman, R. M. 2005. Uncommon cold: could 4°C storage improve platelet function? *Transfusion.* 45:1407–1412.

49. Nesbitt, W. S., E. Westein, …, S. P. Jackson. 2009. A shear gradient-dependent platelet aggregation mechanism drives thrombus formation. *Nat. Med.* 15:665–673.

Supporting material: Enhanced deposition of sickle cells at acute corners and its possible role in vaso-occlusion

Etienne Loiseau
Université Montpellier 2 and CNRS UMR 5221,
Laboratoire Charles Coulomb, Montpellier, F-34095, France

Gladys Massiera
Université Montpellier 2 and CNRS UMR 5221,
Laboratoire Charles Coulomb, Montpellier, F-34095, France

Simon Mendez
Université Montpellier 2 and CNRS UMR 5149,
Institut de Mathématiques et de Modélisation de Montpellier,
Montpellier, F-34095, France

Patricia Aguilar Martinez
Hôpital Saint Eloi,
Laboratoire d'Hématologie, Montpellier, France

Manouk Abkarian[1]
Université Montpellier 2 and CNRS UMR 5221,
Laboratoire Charles Coulomb, Montpellier, F-34095, France

[1]Corresponding author: Manouk.Abkarian@univ-montp2.fr. Address: Université Montpellier 2 and CNRS UMR 5221, Laboratoire Charles Coulomb, Montpellier, F-34095, France, Tel.: 33 (0)4 67 14 39 82, Fax: 33 (0)4 67 14 46 37

1 Method

1.1 Soft lithography

Devices are fabricated using the classical soft-lithography with replica molding method (1). They are made of a silicone elastomer, the polydimethylsiloxane (PDMS) which allows gas exchange (2). The desired design is created with a computer-aided design software (Clewin, WieWeb Software, Netherlands), which we print on a transparency (for ÃŠlargeÃŞ features between 10 and 200 μm) by a high-resolution commercial image setter. This transparency serves as the photomask in contact photolithography. The soft lithography step produces a positive relief of photoresist (SU-8, MicroChem Corp, USA) on a silicon wafer. The speed of the spin-coater sets the thickness of this layer of photoresist, controlling the height of the channels. Then, we pre-bake the wafer for several minutes at 65°C and 95°C (exact times depends on the brand of the photoresist and the desired thickness) in order to initiate the polymerization of the SU-8. A UV source is used to expose the silicon wafer covered with the photomask. Another baking step finishes to cure the photoresist. Dissolving away the non-illuminated — and so the non-polymerized — photoresist leaves a positive relief that serves as a master. Then PDMS channels are formed by replica molding (ridges on the master appear as valleys in the replica). We mix the solution of silicone elastomer with a curating agent (Sylgard 184 kit silicone elastomer, Dow Corning) in a ratio 10/1 and homogenize the mixture. After pouring the solution into a petri dish over the master, we degas under a vacuum in order to get rid of any bubbles. The whole preparation is cured in an oven at 65°C for 1 hour. The replica is then peeled from the master and access holes are punched out of the cured layer by using a truncated needle before assembly.

Since PDMS is porous to gas, we use this feature to control the oxygen concentration in the channels via a two-layer device. The first layer of 60 μm in thickness is engraved with channels of 30 μm high where RBCs flow. This layer is bonded to a glass microslide using a corona discharge for tens of seconds produced by a hand-held discharge unit (Electro-Technic Products, model BD-20AC) with an output voltage of 25 kV. If a rubber-like polymer such as PDMS is placed under such a corona discharge, the charged particles that are generated deposit on the surface, where they initiate radical reactions that modify the rubber surface by creating functional groups (e.g. Si-OH), which are used to bond covalently PDMS to PDMS or to glass. The treatment has to be fast because the PDMS gas permeability decreases while exposed to the corona discharge (3). The second layer, dedicated to the gas flow is bonded on the top of the first one. The channels are 500 μm width and 80 μm high and cover all of the surface of the chip to maximize the gas exchange.

2 Description of the numerical simulations

Two types of computer simulations are performed to support the analysis of the experimental results. First, the flow around a triangular pillar is computed, in the absence of cells. Then, two-dimensional simulations illustrate how deformable objects may interact when flowing around a pillar. All the simulations were performed using YALES2BIO (http://www.math.univ-montp2.fr/-

∼yales2bio), an in-house flow solver developed at the I3M. It is based on the YALES2 solver (http://www.coria-cfd.fr/index.php/YALES2), developed at CORIA, in Rouen (France). YALES2BIO is dedicated to the simulations of blood flows, either with or without the presence of deformable cells (4–6).

2.1 Numerical simulations of the flow around a pillar

The complete geometry of the RBC channel (displayed in figure 1 of the paper) is complex. The ratio between the smallest geometrical length scales and the length of the channel is also very small. A full computation of the flow in the channel would thus be tedious. The objective here is to get information about the flow around one triangular pillar. However, pillars are surrounded by other pillars, which makes the computation of the flow around one isolated pillar irrelevant. It was thus decided to compute an asymptotic case, in which the fluid flows around an infinite number of pillars, arranged in a staggered manner, as in the experiment. In this configuration, it is possible to reduce the computational domain using periodic boundary conditions. Such a technique is classical for computations for channel flows (7) and has also been used for more complex flows (8).

2.1.1 Geometry

The geometry of the computational domain is shown in figure S4. The periodic array of pillars is suggested in the figure by the presence of the neighboring pillars, drawn in dashed lines. Three pairs of periodic boundary conditions delimitate the frontiers of the computational domain (thin solid lines). In the z direction, the computational domain has a height of $h = 30$ μm: it is closed by impermeable walls at $z = \pm 15$ μm. Pillars are staggered in space, the distance between two pillars being $L = 200$ μm. The pillar itself is an isosceles triangle with rounded corners. We denote by c1 the left corner (leading edge) and c2 and c3 the right (downstream) corners. The radius of curvature for the corners is 4 μm for c1 and 5 μm for c2 and c3. The 'heights' of the pillar are 54 μm from c1 to the opposite edge and 50 μm from c2 (resp. c3) to the opposite edge (the angle of c1 is approximately 54 degrees).

2.1.2 Boundary Conditions

Periodic boundary conditions are applied on the three pairs of frontiers of the hexagonal domain (thin solid lines in figure S4). In order to generate the flow, a mean pressure gradient is imposed via a constant source term in the x direction. Non-slipping wall boundary conditions are applied on the pillar surface. In the z direction, non-slipping wall boundary conditions are applied at $z = \pm 15$ μm.

2.1.3 Grid

In order to compute the flow in this periodic domain, it is discretized using tetrahedral cells. The tetrahedral grid used is composed by 2.35 million elements. The grid resolution is set to 2 μm far

from the pillar (near the periodic boundary conditions) and smoothly decreases to reach 1 μm near the pillar. No significant change in the results has been observed by refining the grid.

2.1.4 Model and numerics

In this discretized domain, the incompressible Navier-Stokes equations are solved:

$$\boldsymbol{\nabla}.\vec{u} = 0, \tag{1}$$

$$\rho\,(\frac{\partial \vec{u}}{\partial t} + \vec{u}.\boldsymbol{\nabla}\vec{u}) = -\boldsymbol{\nabla}p + \boldsymbol{\nabla}.[\mu(\boldsymbol{\nabla}\vec{u} + (\boldsymbol{\nabla}\vec{u})^T)] \; + \; S\,\vec{e_x}, \tag{2}$$

where ρ and μ are the constant density and the dynamic viscosity of the fluid, respectively. $\vec{u}$ is the fluid velocity, p the pressure and t the time. The flow is maintained from left to right thanks to an additional source term S in the momentum equation in the x direction. The forced unsteady Navier-Stokes equations are solved using a fourth-order finite-volume scheme. YALES2BIO solves the unsteady Navier-Stokes equations using a projection method. A fourth-order Runge-Kutta scheme is used to advance the velocity field and the Deflated Preconditioned Conjugate Gradient method (6, 9, 10) is used to solve the Poisson equation for pressure.

2.1.5 Operating point

The kinematic viscosity is set to $\nu = \mu/\rho = 1.2 \times 10^{-6}$ m^2.s^{-1}. The source term is adjusted in order to obtain a mean velocity of the order of the ones encountered in the experiment. The bulk velocity is 110 μm.s^{-1}. The resulting flow is in the creeping flow regime: the Reynolds number based on the channel height of h and the bulk velocity is approximately 0.0028. The computation is run for several characteristic times h^2/ν to obtain time-converged results. In order to guarantee the accuracy of the solution, results were double checked by verifying that they match results obtained using a commercial software and a creeping flow hypothesis. In addition, we verified that the three-dimensional flow structure corresponds well to existing data on creeping flows around corners (11).

2.2 Numerical simulations of capsules flowing around the pillar

In order to illustrate how flowing cells may interact while passing around the pillar, 2-D numerical simulations of the dynamics of capsules are performed. Two-dimensional configurations were considered to shorten the calculation times. Some simulation parameters differ from the experimental values. These choices were made to obtain reasonable computational times while keeping the essential ingredients present in the experiment. The 2-D simulations are not an attempt to mimic the experiment. They are to be considered as an illustration of how particles flowing around the pillar corner may interact to explore otherwise forbidden regions of the flow. Numerical simulations of the experiment should include accurate membrane mechanics and membrane viscosity for 3-D

red blood cells, with potential adhesion effects, in a dense suspension and with complex geometry in a large channel and for long characteristic times. Such simulations are out of reach of current softwares, but we hope that the simple computations presented here will motivate groups to study the flows of red blood cells around complex geometries using numerical simulations.

2.2.1 Geometry

The configuration of interest is the flow of inextensible capsules around a pillar, in 2-D. In that case, the geometry and the boundary conditions correspond to the 3-D case described earlier, except that the domain is now infinite in the z direction. The configuration is shown in figure S5(a).

Either one isolated capsule or two capsules, one behind another (as shown in figure S4), are deposited in the flow. The capsules are initially elliptic with the large radius of 4 μm and a small radius of 1 μm (the surface ratio). The corresponding equivalent radius (radius of the circle of same area) is $R = 2.7$ μm. The reduced area (ratio of the capsule area over the area of circle of the same perimeter) is 0.54. In the case with two capsules displayed, the initial distance is between the capsules is 0.5 μm. Capsules are deposited with an initial distance to the wall of 0.75 μm, just upstream of the corner. When capsules are positioned further upstream from the corner, the wall-associated lift has time to act and capsules pass the corner far from the wall.

2.2.2 Boundary conditions

The boundary conditions correspond to what is done in the 3D simulations in the absence of capsule, except in the z direction, which is now infinite. Non-slipping wall boundary conditions are applied at the surface of the pillar. The numerical domaine is delimited by three pairs of periodic boundary conditions (thin solid lines in figure S5a). As in 3D, as there are no inlets/outlets in this configuration, the flow is maintained by imposing a constant source term, as in the previous three-dimensional simulation.

2.2.3 Grid

Computational domains are discretized using unstructured triangular grids. They are refined in the region where the capsules flow, where the grid resolution is of order of 0.3 μm. The membrane is discretized with 64 markers. The order of magnitude of the grid sizes corresponds to what is used in the numerical simulations used to validate the software in the paper by Mendez *et al.* (4).

2.2.4 Model

A fluid-structure interaction method dedicated to the computation of the dynamics of capsules and vesicles under flow is implemented in the YALES2BIO flow solver (4). The Navier-Stokes flow solver described earlier is modified to account for the presence of deformable objects. The method is based on the immersed boundary technique (12, 13) for infinitely thin membranes, initially developed for Cartesian fluid grids and adapted to unstructured finite-volume formulations (4). This method

is a one-fluid method in which forced Navier-Stokes equations are solved everywhere, on a fixed Eulerian grid:

$$\boldsymbol{\nabla}.\vec{u} = 0, \tag{3}$$

$$\rho\,(\frac{\partial \vec{u}}{\partial t} + \vec{u}.\boldsymbol{\nabla}\vec{u}) = -\boldsymbol{\nabla}p + \boldsymbol{\nabla}.[\mu(\boldsymbol{\nabla}\vec{u} + (\boldsymbol{\nabla}\vec{u})^T)] \;+\; S\,\vec{e_x} \;+\; \vec{f}. \tag{4}$$

In order to account for the presence of the particles, a source term $\vec{f}$ modeling the forces exerted by the membrane on the fluid is added in the momentum conservation equation (Eq. 4). This force is calculated on the membrane markers, which are tracked in a Lagrangian way, and then regularized on the Eulerian fluid grid (see Mendez *et al.* (4) for numerical details). This force has an elastic component and a bending component (14) ($\vec{f} = \vec{F}^{leas} + \vec{F}^{bend}$) and is applied only in the vicinity of the membrane. The elastic component is obtained by assuming that two neighboring markers of the membrane are linked by a Hookean spring of elastic modulus E_e. The bending component of the force is calculated from the functional derivative of the Helfrich energy (15):

$$\mathcal{E}_b \;=\; \frac{E_b}{2}\int_S \kappa^2\,dS, \tag{5}$$

where E_b is the membrane bending modulus, κ the curvature (inverse of the radius of curvature; with $\vec{n}$ the outward pointing normal vector to the membrane, $\kappa = \boldsymbol{\nabla}.\vec{n}$). Spontaneous curvature is supposed to be zero. The associated force exerted by the membrane on the fluid reads

$$\vec{F}^{bend} \;=\; E_b\,[\frac{1}{2}\,\kappa^3 \;+\; \Delta_{LB}\,\kappa]\,\vec{n}, \tag{6}$$

where Δ_{LB} is the Laplace-Beltrami operator, *ie*: $\Delta_{LB} = (\mathbf{I}_s\boldsymbol{\nabla}).(\mathbf{I}_s\boldsymbol{\nabla})$ and $\mathbf{I}_s = \mathbf{I} - \vec{n}\vec{n}$ (16).

The capsules deposited are actually almost inextensible and resist bending. Such an object is often referred to as vesicle (14). In 2-D, the difference is minimal. Such 2-D objects are often used in the literature to demonstrate physical phenomena (14, 17–20) relevant to elastic capsules, lipid vesicles or red blood cells. Extensive validation of the solver is presented by Mendez *et al.* (4)

2.2.5 Operating point

In order to accelerate the computation, a bulk velocity of 18 mm.s^{-1} is imposed. In the region where the particles are deposited, the shear k is such that the particle Reynolds number is $k\,R^2/\nu \approx 5 \times 10^{-3}$, which is small and guarantees the absence of inertial lift at the scale the capsules. The capillary number, based on the elastic coefficient of the membrane E_e is $Ca = \mu\,k\,R/E_e = 0.002$, which ensures that the membrane perimeter varies of less than 0.5% during the calculations. The bending coefficient E_b is such that $E_b/(E_e\,R^2) = 0.001$. The viscosity is identical inside and outside the capsule.

2.2.6 Control numerical experiment

A second test case with capsules is used as a control numerical experiment: it is a simple 2-D Couette flow between two flat walls. The configuration is shown in figure S5(b). The Couette domain is a rectangle of length 500 μm and height 100 μm. This domain is used to compare the dynamics of capsules around a corner and along a flat wall. The model, grid resolution and the characteristic parameters (shear rate, capillary number, Reynolds number, bending coefficient) are strictly identical to the case of flowing capsules around a pillar, described in the former subsections. In this Couette flow, the shear rate is constant and identical to the one seen by the capsules when they flow along the lateral wall of the pillar.

Couette flow simulations were used as control cases, to confirm that the specific results obtained around the pillar are related only to the flow geometry. In the Couette flow, capsules simply interact by switching positions, as observed in computations of two interacting vesicles or capsules (21) in the presence of a wall. The specific phenomenon shown in the paper of capsules exploring regions very close to the pillar wall is thus the result of a combination between a geometrical singularity and multi-body effects.

3 Supplemental figures

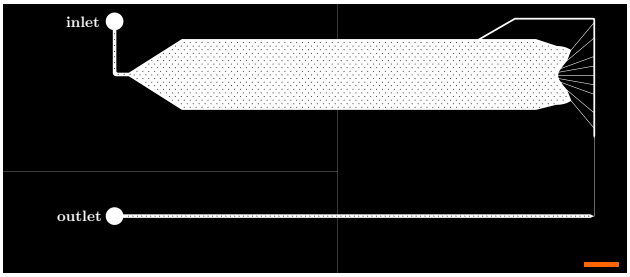

Figure S1: **Geometry of the microfluidic chip 3**.

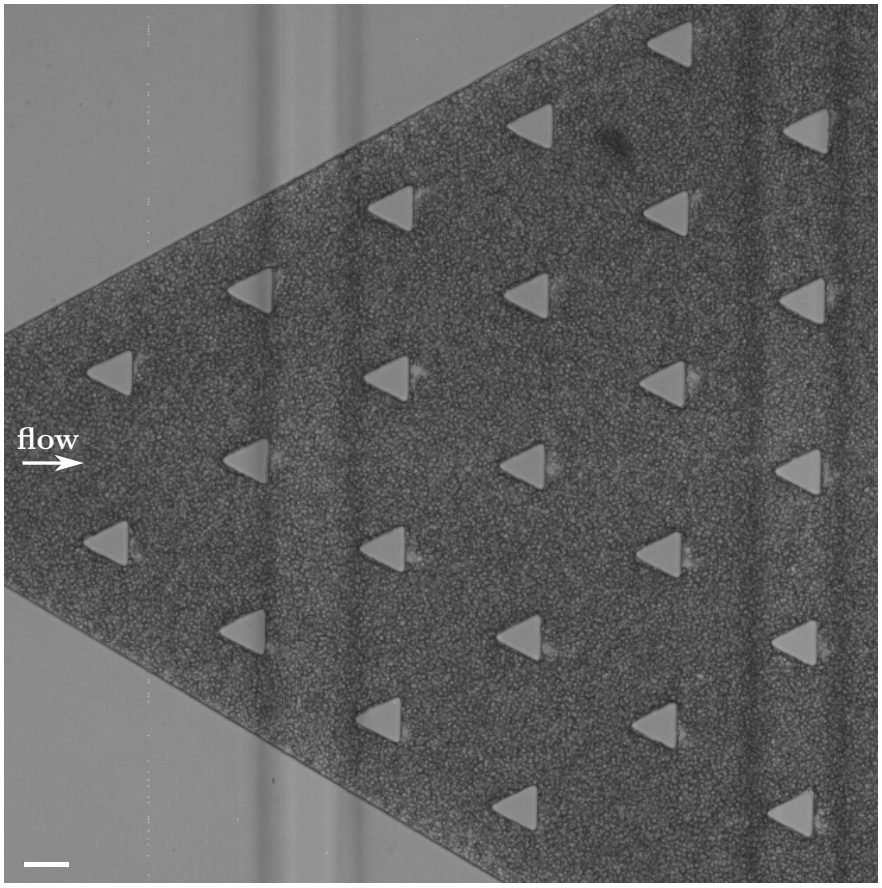

Figure S2: **Absence of aggregation with healthy RBCs.** Picture of the field of view of the microcirculation section of the chip 1 where the triangular posts are present. After 90 minutes of flow, only a few healthy RBCs (sample 11) adhere to the base of the posts. The scale bar is 50 μm.

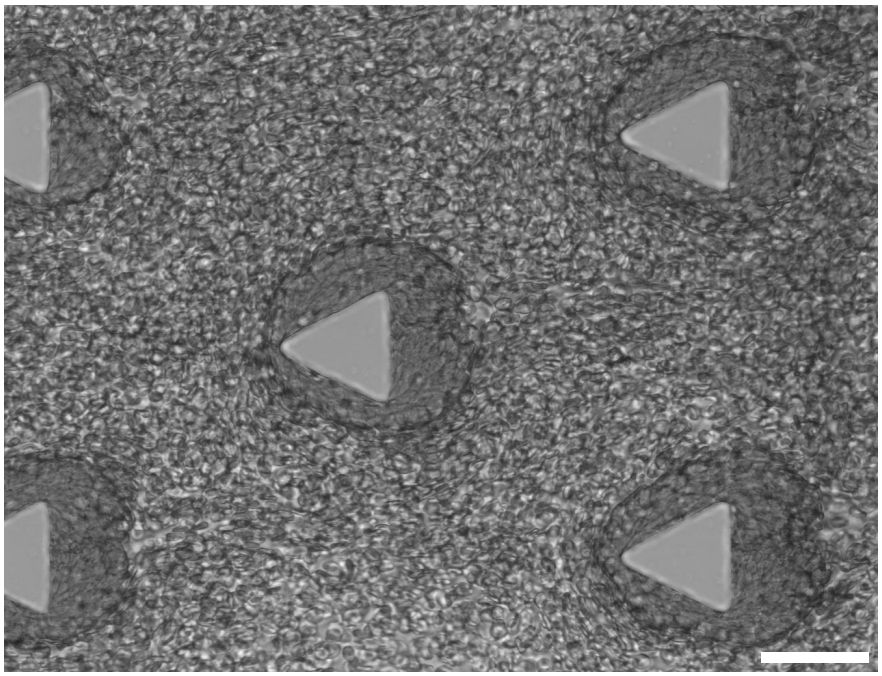

Figure S3: **Aggregate formation under oxygenated conditions.** Picture of the aggregates formed 120 minutes after the initiation of the flow under only oxygenated conditions (sample 4). The scale bar is 50 μm

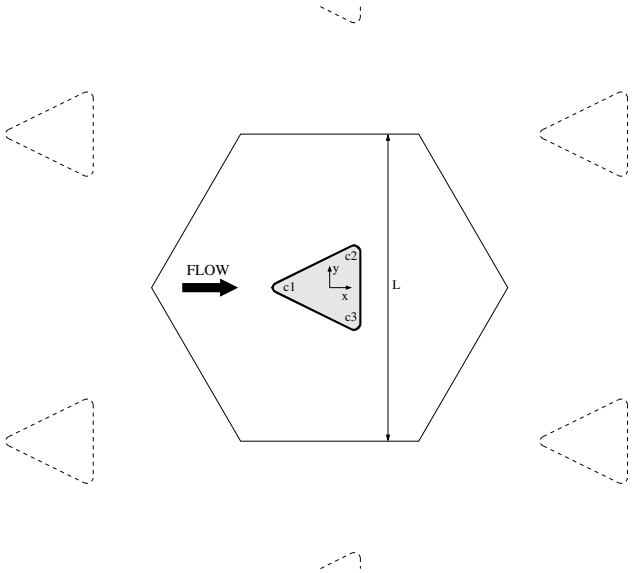

Figure S4: **Schematic of the computational domain (in solid lines) used in the 3-D simulations, over the symmetry plane** $z = 0$. The infinite array of pillars is suggested by the neighboring pillars shotted in dashed lines. In the third direction z (normal to the sheet), the domain is extruded, with wall boundary conditions at $z = \pm 15$ μm.

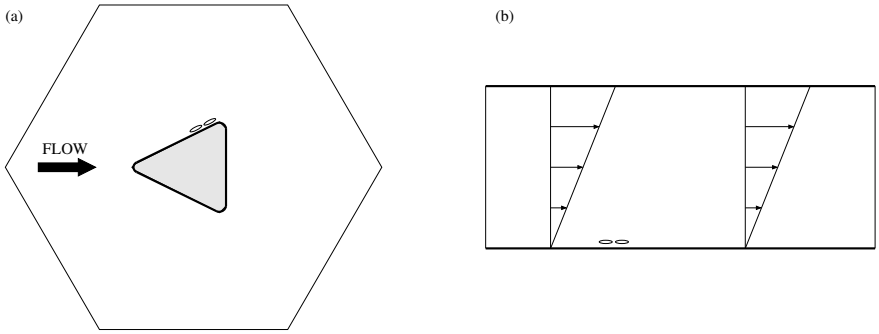

Figure S5: **Two-dimensional configurations used for the dynamics of inextensible capsules near walls**. Thick solid lines are used for solid walls and thin lines for periodic boundary conditions. Two configurations are used: the tri-periodic domain (a) and the Couette flow (b), where the upper wall is moving at prescribed velocity. Small ellipses show the initial locations of the capsules deposited in the flow.

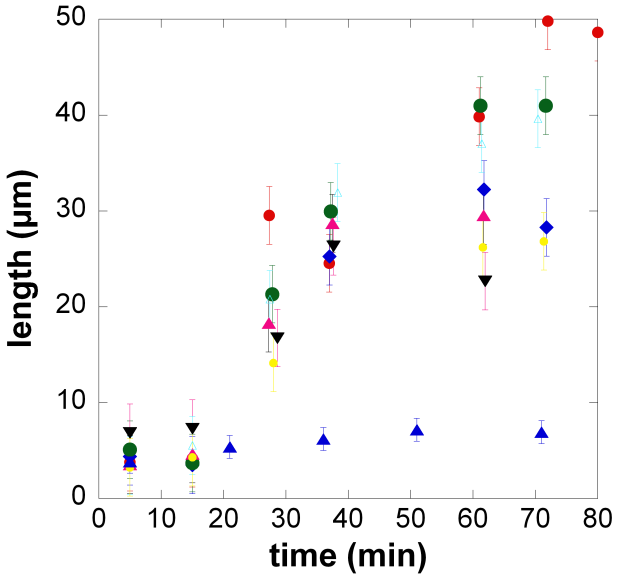

Figure S6: **Temporal evolution of SRBC aggregates at the rear of pillars.** Blood sample from the fraction II, 58% HbS and hematocrit = 25 % in the channels. The blue triangles are for the control experiment with healthy RBCs at the same hematocrit and mean cell hemoglobin concentration.

4 Supplemental movies

movie 1: Timelapse over 1h of aggregation of SRBCs (25% hematocrit, fraction 2, 58% HbS) at the pillar corners, under deoxygenated conditions. The movie start 20 minutes afer the flow has been initiated. First, two aggregates grow at the corners at the rear of a pillar, then after 60 minutes the two aggregates merge together and reach a final size of about 40 μm.
movie 2: Timelapse of SRBCs aggregation under oxygenated conditions. Oxygenated SRBCs are more deformable due to the absence of HbS fibers. This lead to a better alignment of the SRBCs along the the stream flow within the aggregate. Blood sample at 25% hematocrit, fraction II and 58% HbS.
movie 3: Fluctuating aggregate at the rear of a pillar. SRBCs at 25% hematocrit, 58 % HbS and in presence of autologous plasma.
movie 4: detachment of an aggregate from the rear of a pillar. Experimental conditions : SRBCs from the fraction II, 25% hematocrit, 63% HbS.

References

1. Duffy, D., J. McDonald, O. Schueller, and G. Whitesides, 1998. Rapid prototyping of microfluidic systems in poly(dimethylsiloxane). *Anal. Chem.* 70:4974–4984.

2. Vollmer, A., R. Probstein, R. Gilbert, and T. Thorsen, 2005. Development of an integrated microfluidic platform for dynamic oxygen sensing and delivery in a flowing medium. *Lab-on-a-chip* 5:1059–1066.

3. Shiku, H., T. Saito, C. Wu, T. Yasukawa, M. Yokoo, H. Abe, T. Matsue, and H. Yamada, 2006. Oxygen permeability of surface-modified poly(dimethylsiloxane) characterized by scanning electrochemical microscopy. *Chem. Lett.* 35:234–235.

4. Mendez, S., E. Gibaud, and F. Nicoud, 2014. An unstructured solver for simulations of deformable particles in flows at arbitrary Reynolds numbers. *J. Comp. Physics* 256:465–483.

5. Martins Afonso, M., S. Mendez, and F. Nicoud, 2014. On the damped oscillations of an elastic quasi-circular membrane in a two-dimensional incompressible fluid. *J. Fluid Mech.* 746:300–331.

6. Chnafa, C., S. Mendez, and F. Nicoud, 2014. Image-based large-eddy simulation in a realistic left heart. *Comp. Fluids* 94:173–187.

7. Moin, P., and J. Kim, 1982. Numerical investigation of turbulent channel flow. *J. Fluid. Mech.* 118:341–377.

8. Mendez, S., and F. Nicoud, 2008. Large-eddy simulation of a bi-periodic turbulent flow with effusion. *J. Fluid. Mech.* 598:27–65.

9. Moureau, V., P. Domingo, and L. Vervisch, 2011. From Large-Eddy Simulation to Direct Numerical Simulation of a lean premixed swirl flame: Filtered Laminar Flame-PDF modeling. *Comb. and Flame* 158:1340–1357.

10. Malandin, M., N. Maheu, and V. Moureau, 2013. Optimization of the deflated Conjugate Gradient algorithm for the solving of elliptic equations on massively parallel machines. *J. Comp. Physics* 238:32–47.

11. Rusconi, R., S. Lecuyer, N. Autrusson, L. Guglielmini, and H. Stone, 2011. Secondary flow as a mechanism for the formation of biofilm streamers. *Biophys. J.* 100:1392–1399.

12. Peskin, C., 1977. Numerical Analysis of Blood Flow in the Heart. *J. Comp. Physics* 25:220–252.

13. Doddi, S., and P. Bagchi, 2008. Lateral migration of a capsule in a plane Poiseuille flow in a channel. *Int. J. Multiphase Flow* 34:966–986.

14. Ghigliotti, G., T. Biben, and C. Misbah, 2010. Rheology of a dilute two-dimensional suspension of vesicles. *J. Fluid Mech.* 653:489–518.

15. Helfrich, W., 1973. Elastic properties of lipid bilayers: Theory and possible experiments. *Z. Naturforsch.* 28c:693–703.

16. Pozrikidis, C., 2010. Computational Hydrodynamics of Capsules and Biological Cells. *Boca Raton: Chapman & Hall/CRC*.

17. Bagchi, P., 2007. Mesoscale Simulation of Blood Flow in Small Vessels. *Biophys. J.* 92:1858—1877.

18. Ghigliotti, G., H. Selmi, L. El Asmi, and C. Misbah, 2012. Why and how does collective red blood cells motion occur in the blood microcirculation? *Phys. Fluids* 24:101901.

19. Lamura, A., and G. Gompper, 2013. Dynamics and rheology of vesicle suspensions in wall-bounded shear flow. *Europhys. Lett.* 102:28004.

20. Thiébaud, M., Z. Shen, J. Harting and C. Misbah, 2014. Prediction of Anomalous Blood Viscosity in Confined Shear Flow. *Phys. Rev. Lett.* 112:238304.

21. Narsimhan, V., H. Zhao, and E. S. G. Shaqfeh, 2014. Coarse-grained theory to predict the concentration distribution of red blood cells in wall-bounded Couette flow at zero Reynolds number. *Phys. Fluids* 25:061901,1–21.